BIOCHEMISTRY
including biophysical chemistry & molecular biology

ARTICLE

pubs.acs.org/biochemistry

X-ray Absorption Spectroscopy Structural Investigation of Early Intermediates in the Mechanism of DNA Repair by Human ABH2

Nitai Charan Giri,[†] Hong Sun,[‡] Haobin Chen,[‡] Max Costa,[‡] and Michael J. Maroney[*,†]

[†]Department of Chemistry, University of Massachusetts, Amherst, Massachusetts 01003, United States

[‡]Department of Environmental Medicine, New York University School of Medicine, New York, New York 10016, United States

S *Supporting Information*

ABSTRACT: Human ABH2 repairs DNA lesions by using an Fe(II)- and αKG-dependent oxidative demethylation mechanism. The structure of the active site features the facial triad of protein ligands consisting of the side chains of two histidine residues and one aspartate residue that is common to many non-heme Fe(II) oxygenases. X-ray absorption spectroscopy (XAS) of metallated (Fe and Ni) samples of ABH2 was used to investigate the mechanism of ABH2 and its inhibition by Ni(II) ions. The data are consistent with a sequential mechanism that features a five-coordinate metal center in the presence and absence of the α-ketoglutarate cofactor. This aspect is not altered in the Ni(II)-substituted enzyme, and both metals are shown to bind the cofactor. When the substrate is bound to the native Fe(II) complex with α-ketoglutarate bound, a five-coordinate Fe(II) center is retained that features an open coordination position for O_2 binding. However, in the case of the Ni(II)-substituted enzyme, the complex that forms in the presence of the cofactor and substrate is six-coordinate and, therefore, features no open coordination site for oxygen activation at the metal.

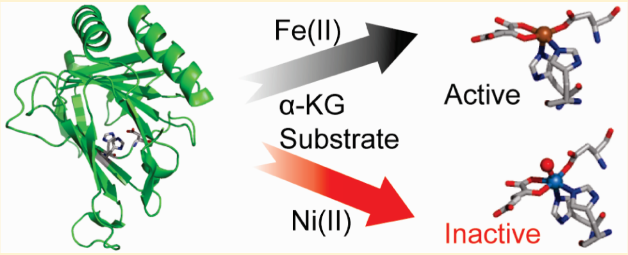

Gene silencing via DNA methylation is part of the normal epigenetic regulation of gene expression.[1−5] Cellular DNA can also sustain damage from alkylation by chemicals that modify DNA bases,[6] and this damage can be inherited.[7] The effects of alkylation damage can be mutagenetic, cytotoxic, or both.[8−10] Cells have evolved systems to repair DNA alkylation damage.[11] *Escherichia coli* has an adaptive response pathway to protect DNA against high levels of alkylation damage.[12] In humans, the enzyme ABH2 plays the role of repairing endogenously formed 1-methyladenine and 3-methylcytosine lesions in duplex DNA.[13]

ABH2 utilizes Fe(II) and αKG to catalyze the oxidative demethylation of methylated DNA bases (Figure 1).[14] Thus, ABH2 belongs to the large class of αKG-dependent non-heme Fe(II) oxygenases that activate O_2 to catalyze the oxidation of a broad range of biological substrates.[15−20] The active site metal is typically bound by a facial triad of protein ligands consisting of the side chains of two histidines and one glutamate or aspartate and water molecules.[15−18,20,21] A crystal structure of the ABH2-αKG complex with the non-native metal ion Mn(II) reveals a six-coordinate structure in which the protein ligands are provided by His171, His236, and Asp173, and the αKG cofactor binds in a bidentate fashion, with the sixth position occupied by an aqua ligand.[22] Prior XAS studies have shown that the native metal ion, Fe(II), is five-coordinate in the resting enzyme.[23]

Substitution of iron with other metals in ABH2 would be expected to yield an enzyme with altered function because of changes in the ability of the metal site to bind and decarboxylate αKG, and/or bind and activate O_2. It has been reported that Ni(II) inhibits ABH2 by replacing the active site metal,[23] although the nature of the mechanistic change is not known. Substitution of the active site Fe(II) ion with Ni(II) has also been proposed to be involved in nickel carcinogenesis via the silencing of tumor suppressor genes.[24,25] Herein, we use XAS as a structural probe of the active site metal center in wild-type (WT) recombinant ABH2 (Fe−ABH2) and Ni(II)-substituted WT recombinant ABH2 (Ni−ABH2) to examine the reaction mechanism and ascertain the intermediate(s) affected by nickel substitution.

■ EXPERIMENTAL PROCEDURES

Expression and Purification of ABH2. The pET28a-His_6-ABH2 vector was obtained from T. R. O'Connor.[13] *E. coli* BL21(DE3)pLysS competent cells (Novagen) were transformed with pET28a-His_6-ABH2 and were plated and grown overnight at 37 °C on LB medium containing 30 μg/mL kanamycin and 34 μg/mL chloramphenicol. Single colonies were grown overnight in 150 mL cultures (LB kanamycin/chloramphenicol) and diluted 1:100 in 2 L of fresh medium. The cells were grown at 37 °C to an optical density of 0.5 at 600 nm and then induced

Received: October 15, 2010
Revised: April 19, 2011
Published: April 21, 2011

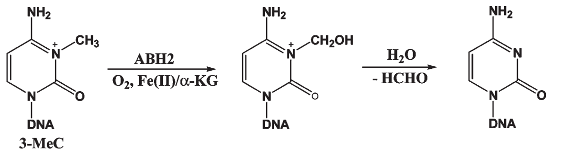

Figure 1. Demethylation of 3-methylcytosine showing the step catalyzed by ABH2.

with isopropyl β-D-1-thiogalactopyranoside (final concentration of 1 mM). The cells were grown for an additional 3 h at 25 °C, harvested by centrifugation, resuspended in lysis buffer [50 mM HEPES, 300 mM NaCl, 2 mM 2-mercaptoethanol, 2 mM EDTA, and 5% glycerol (pH 7.8)], and stored at −80 °C. Upon thawing, the cells were lysed in the presence of PMSF and DNase and then centrifuged to collect the lysate. The lysate was then dialyzed against lysis buffer without EDTA. After dialysis, the soluble proteins were loaded onto a Ni-NTA column. The column was washed sequentially with buffers [50 mM HEPES, 300 mM NaCl, 2 mM 2-mercaptoethanol, and 5% glycerol (pH 7.8)] containing 10, 40, and 60 mM imidazole. Pure protein was eluted using the same wash buffer, but with 250 mM imidazole added. The His$_6$ tag was cleaved from purified protein using a Thrombin CleanCleave Kit (Sigma) and removed by dialysis. Purity was confirmed by a single band with a molecular mass of 33 kDa on a sodium dodecyl sulfate−polyacrylamide gel electrophoresis gel. Apoprotein was prepared via addition of a 5-fold excess of EDTA to the protein solution and incubation at 4 °C overnight. The EDTA was then removed by dialysis against a buffer solution containing 50 mM HEPES, 100 mM NaCl, and 2 mM ascorbic acid (pH 7.8). Protein concentrations were determined by the Bradford assay[26] using BSA as a standard. Metallated samples were prepared in a Coy chamber and frozen under a N_2 atmosphere. Fe−ABH2 was prepared via addition of a solution of $(NH_4)_2FeSO_4$ (10 mM, 1.25 equiv) in the buffer described above to 18 μM apoprotein and incubation for 6 h. Unbound and nonspecifically bound iron was then removed via addition of Chelex 100 beads to the sample, incubation for 20 min, and then decanting the solution via pipet. The demethylase activity of the samples was confirmed using an assay described previously[23] (see the Supporting Information).

The same procedure, only substituting $Ni(OAc)_2$ for $(NH_4)_2FeSO_4$, was used to prepare Ni−ABH2.

XAS Sample Preparation. From the Fe−ABH2 preparation described above, a total of three samples were prepared for XAS experiments. The first sample contained only the metallated protein, hereafter termed Fe−ABH2. The second sample contained Fe−ABH2 and 1.0 equiv of αKG, hereafter termed Fe−ABH2−αKG. Finally, the third sample contained Fe−ABH2, 1.0 equiv of αKG, and 5 equiv of a substrate, 5′-AAAGCAC-MeCGGTCGAAAAAGCGAAA-3′ (MeC being 3-methylcytosine; Midland Certified Regent Co.; $K_m \sim 4-5\ \mu M$[27]), and is hereafter termed Fe−ABH2−αKG + substrate. The samples had an iron content of ∼0.3 mM, as determined by ICP-OES. Three analogous samples were prepared from Ni−ABH2 (vide supra). The samples had a nickel concentration of ∼0.3 mM. On the basis of a Bradford assay of protein concentration, the samples had metal:protein ratios of 0.89:1 (Fe−ABH2) and 0.93:1 (Ni−ABH2). The samples were added via syringe to polycarbonate sample holders with kapton windows and frozen in liquid N_2 for XAS data collection.

X-ray Absorption Spectroscopy. XAS data collection and analysis were performed as reported previously.[28] Iron and nickel *K*-edge data were collected at 10 K using a liquid He cryostat (Oxford Instruments) on beamline 9-3 at the Stanford Synchrotron Radiation Laboratory. The ring conditions were 3 GeV and 80−100 mA. Beam line optics consisted of a Si(220) double-crystal monochromator and two Rh-coated mirrors for focusing and harmonic rejection. X-ray fluorescence was collected using a 30-element Ge detector (Canberra), with the exception of Fe−ABH2−αKG + substrate, for which a 100-element detector was employed. The data obtained using the latter detector have a significantly higher signal:noise ratio than other data collected at the Fe *K* edge and allowed for a higher-resolution analysis. Scattering was minimized by placing a set of Soller slits with a Z-1 element (Mn or Co) filter between the sample chamber and the detector. X-ray absorption near-edge spectroscopy (XANES) data were collected from −200 to 200 eV with respect to the edge energy of the absorbing metal. The energy of each metal *K* edge was calibrated to the first inflection point of the relevant metal foil (7112.5 eV for Fe and 8331.6 eV for Ni). Extended X-ray absorption fine structure (EXAFS) data were collected to $k = 16$ Å^{-1} for Ni−ABH2 and $k = 14$ Å^{-1} above the edge energy for all other samples.

XAS data analysis was performed using EXAFS123[29] for XANES analysis and SixPack[30] for EXAFS analysis. Scattering parameters for SixPack fitting were generated using the FEFF 8 software package.[31] For the data shown, 18 scans were averaged for Fe−ABH2 and 12 scans were averaged for Fe−ABH2−αKG and Fe−ABH2−αKG + substrate; five scans were averaged for Ni−ABH2 and Ni−ABH2−αKG, and nine scans were averaged for Ni−ABH2−αKG + substrate. The averaged spectra were background corrected and normalized in SixPack, which uses the AUTOBK routine of IFEFFIT.[30,32,33] For XANES analysis, the edge energy reported was taken to be the maximum of the first derivative of the XANES spectrum. For pre-edge XANES analysis, a 75% Gaussian and 25% Lorenzian function was used to fit the rise in the fluorescence at the edge. Gaussian peaks were added to the pre-edge fit to account for any peaks in the pre-edge region, and the areas of these peaks were taken as a measure of their intensities (see the Supporting Information). The intensity of the peak associated with a 1s → 3d electronic transition was then used to indicate the coordination number and/or geometry of metal sites.[34−36] For Ni XANES analysis, the presence or absence of a feature associated with a 1s → 4p$_z$ transition is also useful in identifying complexes with five-coordinate pyramidal or four-coordinate planar geometries.[34]

For EXAFS analysis, the averaged spectra were first converted to *k* space. For the purpose of comparison, all of the data for each metal *K* edge were refined over the same limits, which were determined by the sample with the poorest signal:noise ratio. For Ni *K*-edge data, EXAFS data were fit over a *k* range of 2−12.5 Å^{-1}. For data collected at the Fe *K* edge, a limit of 2−12 Å^{-1} was used. The primary effect of truncating the data is to lower the resolution of similar shells in the fits. For data that would support a higher-resolution analysis, fits employing all the usable data (maximum resolution) were also performed (see the Supporting Information). Structural models of the metal sites involving coordination numbers from 2 to 7 were systematically evaluated for all possible combinations of N/O and S donors by holding the number of scattering atoms in each shell to integer values (see the Supporting Information). The number of histidine imidazole ligands involved in the coordination sphere was estimated by multiple-scattering analysis as previously described.[37−39] Amplitudes and phase shifts for multiple scattering paths for

Table 1. XAS Analysis of ABH2 Samples

	XANES analysis			EXAFS analysis						
sample	edge E (eV)	1s → 3d peak area (×10^{-2} eV)	coordination number	shell	r (Å)^a	σ^{2b} (×10^{-3} Å^2)	ΔE_0 (eV)	%R^c	reduced χ^2	ref
Fe–ABH2 (k = 2–13 Å^{-1})	7125.9(2)	9(1)	5	3 N/O	1.95(2)	0(2)	−8(3)	10.45	97.44	23
				2 N/O (2 Im)	2.08(2)	2(2)				
				3 N/O (2 Im)	2.09(3)	5(2)	−4(3)	10.14	56.8	this work
				1 O	[1.88(2)]^d	2(1)				
				1 O	[1.99(2)]^d					
				1 C	[2.66(2)]^d					
				1 C	[2.75(2)]^d					
Fe–ABH2–αKG (k = 2–14 Å^{-1})	7122.5(2)	14.5(7)	5	2 N/O	1.96(3)	3(2)	−15(2)	2.96	53.86	this work
				3 N/O (2 Im)	2.08(2)	4(3)				
				3 N/O (2 Im)	2.06(2)	1(1)	−5(2)	2.07	36.33	this work
				1 O	[1.94(2)]^d	4(1)				
				1 O	[2.15(2)]^d					
				1 C	[2.66(2)]^d					
				1 C	[2.76(2)]^d					
Fe–ABH2– αKG + substrate (k = 2–12 Å^{-1})	7121.5(2)	10.5(6)	5	2 N/O	1.85(3)	3(2)	−30(5)	17.15	82.04	this work
				3 N/O (2 Im)	2.04(3)	4(2)				
				3 N/O (2 Im)	1.93(3)	4(2)	−14(5)	5.8	42.36	this work
				1 O	[1.85(2)]^d	11(3)				
				1 O	[2.06(2)]^d					
				1 C	[2.57(2)]^d					
				1 C	[2.67(2)]^d					
Ni–ABH2 (k = 2–12.5 Å^{-1})	8344.7(2)	5(1)	5	5 N/O (2 Im)	2.08(2)	5(1)	−4(1)	2.3	8.03	23
				3 N/O (2 Im)	2.05(2)	2(1)	1(3)	4.1	16.45	this work
				1 O	[1.86(4)]^d	5(4)				
				1 O	[1.91(4)]^d					
				1 C	[2.53(4)]^d					
				1 C	[2.55(4)]^d					
Ni–ABH2– αKG (k = 2–14 Å^{-1})	8345.3(2)	5.4(8)	5	5 N/O (2 Im)	2.10(2)	6(1)	−6(1)	3.15	48.82	23
				3 N/O (2 Im)	2.08(2)	2(1)	1(2)	1.35	22.47	this work
				1 O	[1.89(2)]^d	9(2)				
				1 O	[1.94(2)]^d					
				1 C	[2.56(2)]^d					
				1 C	[2.58(2)]^d					
Ni–ABH2– αKG + substrate (k = 2–14 Å^{-1})	8343.5(2)	3.6(7)	6	2 N/O	2.08(2)	3(1)	−4(2)	3.82	468.9	this work
				4 N/O (2 Im)	2.02(8)	10(7)				
				4 N/O (2 Im)	2.04(2)	2(1)	6(1)	2.34	60.22	this work
				1 O	[2.07(2)]^d	3(2)				
				1 O	[2.12(2)]^d					
				1 C	[2.74(2)]^d					
				1 C	[2.76(2)]^d					

[a] r is the radial distance between the metal and ligand. [b] σ^2 is the root-mean-square disorder in the metal–ligand distance. [c] R is the goodness of fit. Numbers in parentheses represent the standard deviation for least-squares fits. [d] Distances in brackets correspond to atoms in a O-C-C-O chelate ring and were constrained to vary with a single value of Δr for the chelate ring.

Fe−Im ligands were generated using FEFF (version 8.0) with the coordinates of an Fe−Im ligand obtained from the crystal structure of human PHF8 with Fe(II) and αKG [Protein Data Bank (PDB) entry 3K3O]. For Ni−Im ligands, the crystal structure of JMJD2A with Ni(II) and substrate bound (PDB entry 2Q8C) was used. Scattering paths of similar length were combined in one shell, as described by Tierney et al.[38,39] Therefore, no single label can be meaningfully applied to these combined paths. During the fitting process, coordination numbers were constrained to be integer values and a scale factor of 0.9 was used. Bond lengths, σ^2, and a single value of ΔE_0 were allowed to vary in each fit. For αKG and ascorbate ligands, fits including imidazole ligands were initially screened for the presence of additional second-coordination sphere C atoms not identified by His ligands using individual single scattering C atoms at ∼2.5 and ∼3.1 Å, respectively (see the Supporting Information). The distances for the αKG C atoms were obtained from the crystal structures of human PHF8 with Fe(II) and αKG (PDB entry 3K3O) and from JMJD2A with Ni(II), substrate, and αKG bound (PDB entry 2Q8C). The crystal structure of the iron complex of trimethylreductic acid (an ascorbic acid analogue)[40] was used for the ascorbate model. The best models using single-scattering C atoms were further examined using multiple-scattering analysis derived from rigid O-C-C-O five-member chelate rings with parameters obtained using FEFF (version 8.0) and the structures mentioned above (Table 1). In this analysis, distances in the chelate ring were constrained to vary with a single value of Δr and σ^2. In all cases where single scattering indicated the presence of second-coordination sphere C atoms, the fits were improved by the substitution of two N/O donors in the first coordination sphere by the chelate ring, which adds two C atoms to the second coordination sphere.

To compare different fits to the same data set, ifeffit uses three goodness of fit parameters, χ^2 (eq 1), reduced χ^2, and R

$$\chi^2 = \frac{N_{\mathrm{idp}}}{N_{\varepsilon^2}} \sum_{i=1}^{N} \{[\mathrm{Re}(f_i)]^2 + [\mathrm{Im}(f_i)]^2\} \qquad (1)$$

where N_{idp} is the number of independent data points, N_{ε^2} is the number of uncertainties to minimize, $\mathrm{Re}(f_i)$ is the real part of the EXAFS fitting function, and $\mathrm{Im}(f_i)$ is the imaginary part of the EXAFS fitting function. Reduced $\chi^2 = \chi^2/(N_{\mathrm{ind}}N_{\mathrm{varys}})$ (where N_{varys} is the number of refining parameters) and represents the degrees of freedom in the fit. ifeffit also calculates R for the fit, which is given by eq 2 and is scaled to the magnitude of the data, making it proportional to χ^2.

$$R = \frac{\sum_{i=1}^{N} \{[\mathrm{Re}(f_i)]^2 + [\mathrm{Im}(f_i)]^2\}}{\sum_{i=1}^{N} \{[\mathrm{Re}(\tilde{\chi}\mathrm{data}_i)]^2 + [\mathrm{Im}(\tilde{\chi}\mathrm{data}_i)]^2\}} \qquad (2)$$

To compare different models (fits), the R factor and reduced χ^2 parameters can be assessed, in which case both parameters should be minimized. Although R will always improve with an increasing number of shells (adjustable parameters), reduced χ^2 will go through a minimum and then increase, indicating that the model is overfitting the data. Best fits were judged by using two goodness of fit parameters, reduced χ^2 and R, and the deviation of σ^2 from typical values.

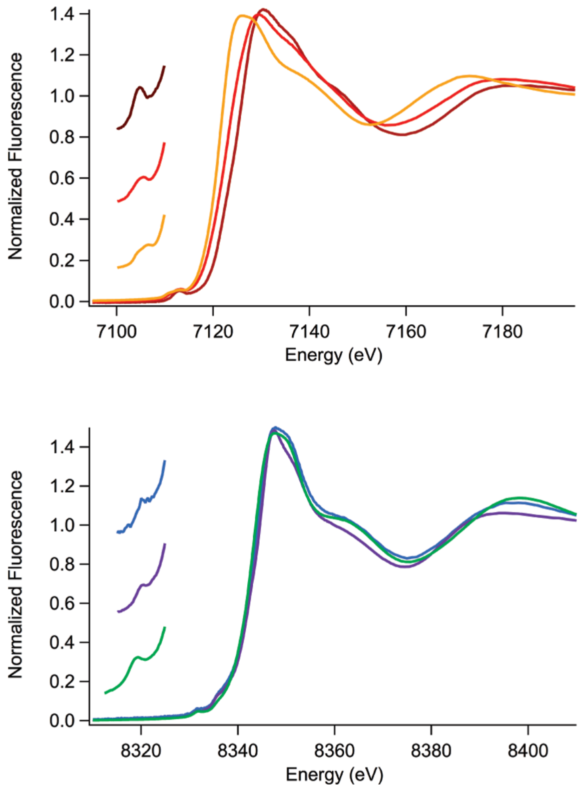

Figure 2. Fe *K*-edge XANES spectra (top): Fe−ABH2 (brown), Fe−ABH2−αKG (red), and Fe−ABH2−αKG + substrate (orange). Ni *K*-edge XANES spectra (bottom): Ni−ABH2 (blue), Ni−ABH2−αKG (purple), and Ni−ABH2−αKG + substrate (green). Inserts show expansions of the pre-edge XANES region showing peaks associated with 1s → 3d electronic transitions.

■ RESULTS

XANES Analysis. XAS experiments were performed to investigate the structures of Fe(II) and Ni(II) bound to ABH2 and upon addition of cofactor or cofactor and substrate. The analysis of XANES data provides information about the coordination number and geometry of a metal site.[34−36] Both Fe(II) and Ni(II) have vacancies in the 3d manifold that give rise to peaks associated with 1s → 3d electronic transitions that are observed in the pre-edge XANES region of the *K*-edge spectra in all the ABH2 samples (Figure 2 and the Supporting Information). The peak areas (intensities) of the 1s → 3d transitions depend on the coordination number and geometry of the metal sites.[34−36] By comparing the 1s → 3d transition peak areas of the ABH2 samples with typical values for known coordination numbers and/or geometries, we were able to determine the coordination numbers of all six ABH2 samples from the XANES data. EXAFS analysis also provides a measure of the number of ligands present in the primary coordination sphere (N), and in all of the cases presented, the determined N values are in agreement with the XANES analysis.

Comparisons of XANES data (Table 1 and Figure 2) for the three iron-containing samples show that each spectrum is distinct. Thus, the structure of the iron site is sensitive to the presence of both αKG and the substrate. There is a systematic shift to a lower *K*-edge energy from Fe−ABH2 to Fe−ABH2−αKG to Fe−ABH2−αKG + substrate that indicates an increase in electron density at the iron site in each of

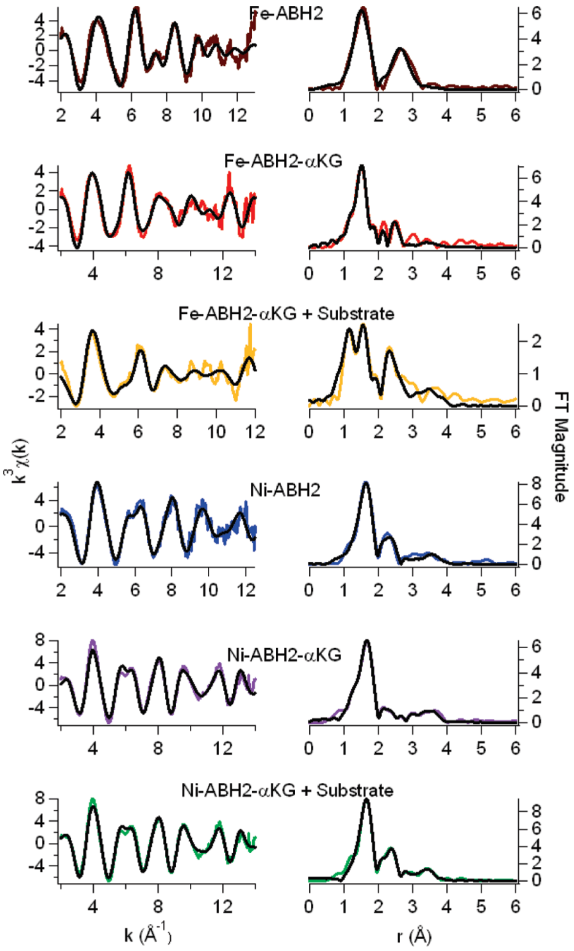

Figure 3. EXAFS analysis. On the left are unfiltered, k^3-weighted EXAFS spectra (colored lines) and fits (black lines, from Table 1). On the right are Fourier-transformed EXAFS data and fits.

these samples. The edge energy observed for Fe−ABH2 [7125.9(2) eV] is very high for Fe(II), more typical of Fe(III) complexes [e.g., 7124 eV for Fe(III) protocatechuate 3,4-dioxygenase (PCD),[41] 7126.6 eV for a hexaquo Fe(III) model complex,[42] and 7125.7 eV for a non-heme (alkylperoxo)Fe(III) intermediate[43]] and higher than those for other non-heme Fe(II) enzymes [e.g., 7120.5 eV for Fe(II)PCD[44]]. In addition, the magnitude of the edge energy shift from Fe−ABH2 to Fe−ABH2−αKG is quite large [3.4(4) eV] and could be interpreted as a reduction of Fe(III) to Fe(II). However, the samples were prepared anaerobically and under reducing conditions (2 mM ascorbate) where no Fe(III) should be present. Thus, formation of Fe(III) in the enzyme would require some redox center intrinsic to the protein. Further, X-band EPR spectra obtained on one of the samples of Fe−ABH2 used for XAS did not exhibit $g = 4.3$ or $g \sim 2$ features (see the Supporting Information), suggesting that little, if any, Fe(III) is present. Another possible explanation might be that the ligand envionment, which is composed of three O donors (including ascorbate) and two N donors (vide infra), leads to an unusually ionic environment that has a high positive charge on the Fe center. In either event, the observed shifts to lower energies would be expected for a site that will eventually bind and reductively activate O_2. No changes in the coordination number of the Fe(II) center are apparent upon binding of the αKG cofactor or upon binding of the substrate to Fe−ABH2−αKG. In all three samples, a peak associated with the 1s → 3d transition is observed near 7113 eV. In the resting sample, Fe−ABH2, the 1s → 3d peak area (∼9 × 10^{-2} eV) is indicative of a five-coordinate complex (typical values are ∼8−13 × 10^{-2} eV).[35,36] The complex remains five-coordinate with a 1s → 3d peak area of ∼14 × 10^{-2} eV upon addition of αKG. Addition of the substrate decreases the 1s → 3d peak area to ∼10 × 10^{-2} eV, a value that is still consistent with a five-coordinate site.

Unlike Fe, which remains five-coordinate in all of the ABH2 samples, Ni−ABH2 shows a change in coordination number upon binding of the substrate. Again, the spectrum of each nickel-containing sample is distinct. However, the Ni *K* edge shows no systematic shift to lower energies upon binding of αKG or the substrate (Table 1), indicating that little change in electron density of the Ni(II) site occurs in response to binding αKG or substrate. Like the analogous iron complexes, XANES analysis shows that Ni−ABH2 has a five-coordinate Ni(II) site [1s → 3d peak area (near 8332 eV) of ∼5 × 10^{-2} eV, typical range of 4−10 × 10^{-2} eV[34]] that remains five-coordinate upon binding of αKG (1s → 3d peak area ∼5 × 10^{-2} eV). However, when the substrate binds, the Ni(II) site becomes six-coordinate, with a decrease observed in the 1s → 3d peak area to 3−4 × 10^{-2} eV; the typical range for six-coordinate Ni complexes is 0.6−4 × 10^{-2} eV [34]. In cases of samples with five-coordinate Ni(II) sites, additional small shoulders near 8338 eV that are associated with 1s → $4p_z$ transitions may be observed. Shoulders corresponding to these transitions are observed for Ni−ABH2 and Ni−ABH2−αKG, but not for Ni−ABH2−αKG + substrate, consistent with the change in coordination number from five for Ni−ABH2 and Ni−ABH2−αKG to six for Ni−ABH2−αKG + substrate (Figure 2 and the Supporting Information).[34] In addition, observation of these features indicates a geometry that is closer to a square pyramidal than to trigonal bipyramidal[34] for the five-coordinate complexes.

EXAFS Analysis. The analysis of EXAFS provides information about the number and types of ligands bound to a metal and metric details of the metal site structure. This information is obtained from the best fits of the data and is summarized in Figure 3 and Table 1. The best fit for Fe−ABH2 EXAFS data consists of five N/O donor ligands, of which two are imidazoles from multiple-scattering analysis (Table 1). This result is consistent with the crystal structure of Mn−ABH2[22] and with the active site structures of other resting non-heme Fe-dioxygenase enzymes,[45] which show ligation by the two-His, one-carboxylate (Asp or Glu) facial triad and water molecules. Fits obtained using single-scattering C atoms in the second coordination sphere indicated the presence of two to three second-sphere carbon atoms for Fe−ABH2 in addition to those associated with two imidazole ligands. Given the prior crystal structure of Mn−ABH2 showing the position of the carboxylate carbon of Asp173 (Mn−C distance of ∼2.97 Å[22]), only one of these C atoms could be assigned to the carboxylate C atom. The other carbon atoms can be attributed to the carbon atoms from a coordinated ascorbate ligand.[46,47] Multiple-scattering analysis derived from the rigid O-C-C-O five-member chelate ring was performed to further test the fit indicating the presence of ascorbate, which is based on the presence of second-coordination sphere C atoms in the models with single-scattering C atoms (see the Supporting Information). These fits use a single distance parameter to position all the atoms in the chelate, and a single

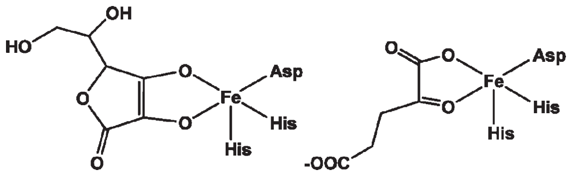

Figure 4. Comparison of the complexes of ascorbate and α-ketoglutarate with the Fe(II) site in ABH2.

value of σ^2 for the ligand, and thus do not contain more adjustable parameters than the corresponding fit without the C atoms. The results show that the qualities of the fits (both R and χ^2) are improved by the replacement of two first-coordination shell N/O donors by one O-C-C-O unit (Table 1). The crystal structure of iron bound to tetramethylreductic acid shows that carbon atoms in the chelate ring are ∼3.0 Å from the iron centers.[40] Using the chelate model, C atoms are found at ∼2.7 Å (Table 1). Note that the model obtained from the crystal structure features two M−C distances, and this was used without modification. The difference in the M−C distance is below the resolution of the EXAFS data and coupled with the errors indicates that the difference in the distances to the C atoms is not resolved. Thus, in the resting iron enzyme prepared in the presence of ascorbate, the aqua ligands are replaced with a bidentate ascorbate ligand (Figure 4). The addition of a third C atom to model the C atom from the aspartate ligand does lead to a significant improvement in the fit (see the Supporting Information).

When ABH2 was reconstituted with Ni(II), the same buffer containing ascorbate was used, but the Ni *K*-edge EXAFS lacks the features associated with the extra C atoms in the FT-EXAFS spectrum (Figure 3). The fit obtained using an O-C-C-O chelate ring is worse that that obtained using only the ligand donor atoms (Table 1). Thus, there is no indication that ascorbate binds to Ni−ABH2, and the Ni(II) site is best modeled by two His imidazoles, one carboxylate, and two aqua ligands.

Addition of αKG to metallated ABH2 (Fe or Ni) results in changes in the EXAFS spectra arising from scattering atoms in both the first and second coordination spheres in the Fourier-transformed spectra (Figure 3). These changes are consistent with the binding of αKG in a bidentate fashion, where changes in the primary coordination sphere reflect the ligand exchange, and the observation of C atoms in the second coordination sphere arises from the ordering of all the atoms in the five-member chelate ring. Although the improvement in the fit is not as dramatic as that for the addition of ascorbate to Fe−ABH2, both R and χ^2 are improved in every case (Table 1). The distance observed for the two C atoms in the model incorporating a five-member chelate ring is ∼2.66 − 2.76 Å (Figure 4) and is similar to that observed in the crystal structure of human PHF8 complexed with αKG (2.47−2.57 Å)[48] and TauD complexed with Fe(II) and substrate (2.57−2.85 Å).[49] Again, the addition of a third C atom to model the aspartate β-C atom does not lead to significant improvements in the fit (see the Supporting Information).

Addition of substrate to the Fe− or Ni−ABH2−αKG complex results in additional structural perturbations, particularly for the Fe sample (Figure 3). The best fits of the EXAFS data suggest the presence of five N/O donor ligands for Fe(II)−ABH2−αKG + substrate, but six N/O donors for Ni(II)−ABH2−αKG + substrate, in agreement with the XANES analysis (Table 1).

Scheme 1. Consensus Mechanism of Non-Heme Fe(II) Oxygenases

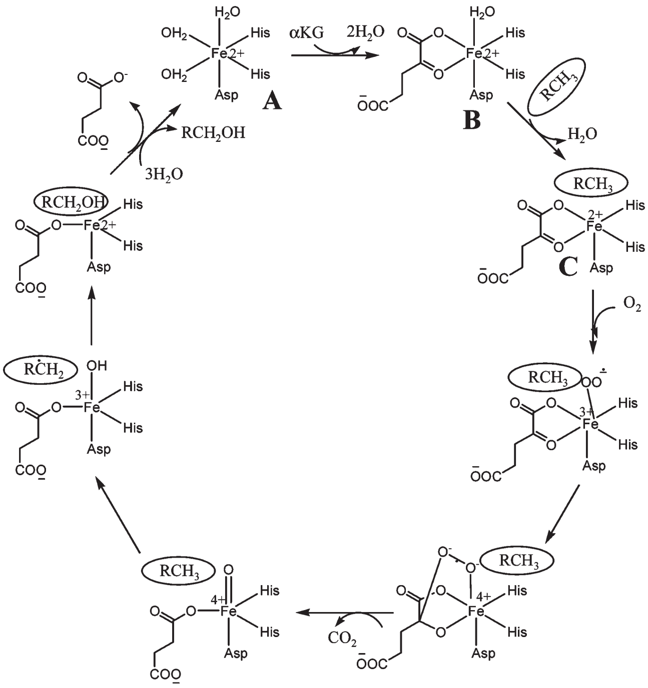

The O-C-C-O five-member chelate rings seen for the αKG complexes are retained when the substrate is added. The best fit for Fe−ABH2−αKG +substrate shows the presence of two second-sphere carbon atoms at ∼2.6−2.7 Å. Similarly, the best fit for Ni−ABH2−αKG + substrate also shows the presence of two second-coordination sphere carbon atoms at a distance of ∼2.75 Å. Again, the addition of a C scatterer to model the aspartate β-C does not significantly improve the fits (see the Supporting Information). Curiously, the best fit for Fe−ABH2−αKG + substrate also shows one very short N/O−Fe distance of ∼1.85 Å, a distance ∼0.09 Å shorter than the distance in Fe−ABH2−αKG. While shorter than that found in the Fe−ABH2−αKG fit, similar distances have been observed in crystal structures of non-heme iron halogenase (1.87 and 1.73 Å),[50] in clavaminate synthase (1.80 Å),[51] and in TauD (1.73 Å).[49] The shortening of these bonds may indicate increased covalency between Fe(II) and αKG and may account in part for the observed decrease in *K*-edge energy observed upon substrate binding.

■ DISCUSSION

ABH2 is a member of a group of Fe(II)- and αKG-dependent dioxygenases that use the 2-His-1-carboxylate motif to bind the metal cofactor. Previously, we reported that ABH2 and JMJD2A are sensitive to Ni(II) ion inhibition.[23] This inhibition may lead to defective DNA demethylation and mutations in the case of ABH2 inhibition, or gene silencing by JMJD2A inhibition; the latter is consistent with the known epigenetic mechanism of nickel carcinogenesis.[24,25] XAS was used to examine the structures of Fe(II)− and Ni(II)−ABH2 complexes for further mechanistic insights. Characterization of a number non-heme Fe(II) oxygenases have revealed that they operate by a sequential reaction mechanism that is designed to prevent reductive oxygen

Scheme 2. Variation of the Consensus Mechanism for ABH2

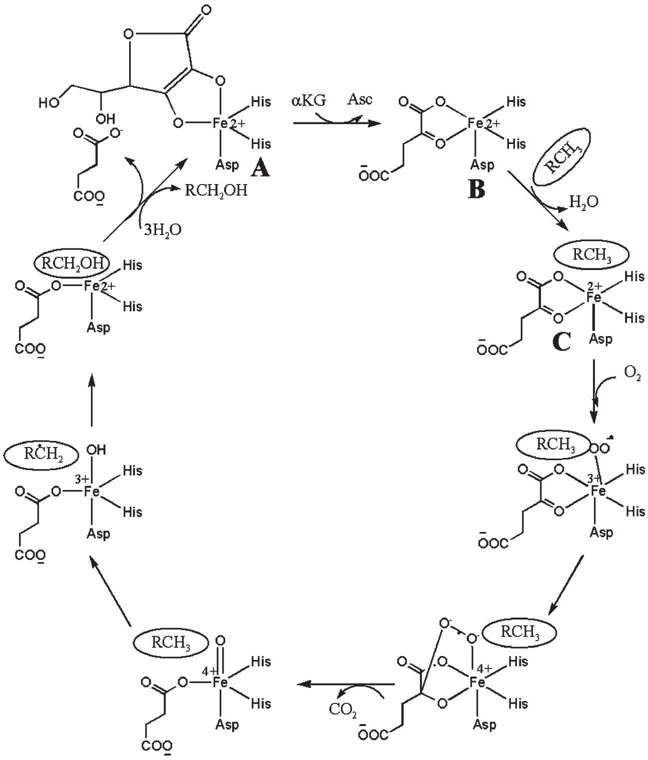

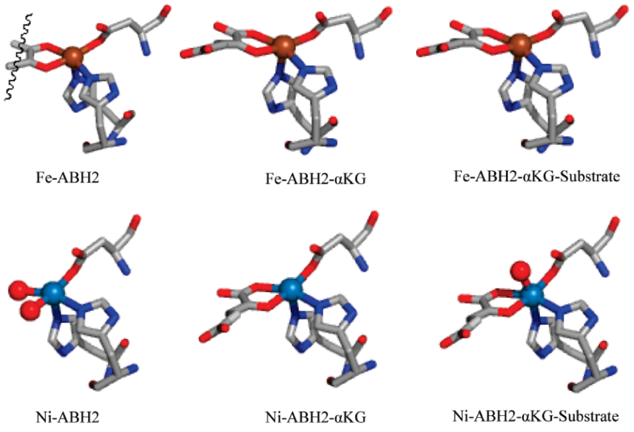

Figure 5. Proposed structures of the Fe and Ni sites of ABH2. M−ABH2 (left), M−ABH2 in the presence of αKG (middle), and M−ABH2 in the presence of both αKG and substrate (right). Iron is colored brown, nickel cyan, carbon gray, oxygen red, and nitrogen blue.

activation until the ternary complex (composed of enzyme, αKG cofactor, and substrate) has formed (Scheme 1).[16,52−54] In the first step of the consensus mechanism, αKG binds in a bidentate fashion to the six-coordinate metal site composed of the 2-His-1-carboxylate facial triad and three aqua ligands (Scheme 1, A), displacing two aqua ligands (Scheme 1, B). This step is followed by binding of the substrate to a site close to the active site metal. The presence of both substrate and cofactor induces the loss of the remaining aqua ligand, which opens a coordination site that serves to bind O_2 (Scheme 1, C). Thus, the saturation of the coordination sphere of the Fe(II) center is used to prevent O_2 binding. Subsequently, oxidative decarboxylation of αKG takes place, leading to the formation of an Fe(IV)=O species.[15] This high-valent iron species is the oxidant involved in catalysis. In the case of ABH2, the Fe(IV)=O species will hydroxylate the methyl group on the N atom of the DNA base. The resulting alcohol then undergoes a further spontaneous reaction to yield formaldehyde and the dealkylated base (Figure 1).

Fe−ABH2 appears to operate by a variation of the consensus mechanism (Scheme 2). XANES and EXAFS analysis are consistent with a five-coordinate site composed of N/O donor ligands for both Fe(II) and Ni(II) in ABH2 in the absence of cofactor or substrate (Scheme 2, A). Analysis of features from scatterers in the second and third coordination shells indicates that two of these ligands are His imidazoles, consistent with the available crystallographic data, and the remaining ligands are presumably derived from Asp and water. The data from the complexes formed with αKG are consistent with the cofactor binding to both metals in a bidentate fashion, while retaining the five-coordinate geometries of the complexes (Scheme 2, B). Thus, αKG displaces two ligands, presumably aqua ligands, from the resting complex. Similar results have been reported by Scott and co-workers with TfdA, where no change in coordination number was observed for the Cu− or Fe−TfdA complex upon addition of αKG.[37] Therefore, binding of αKG does not change the coordination number of the metal center but perturbs the electronic environment of the metal center by substituting for other ligands (e.g., aqua or ascorbate). Upon binding substrate, the Fe(II) site remains five-coordinate (Scheme 2, C). However, the *K*-edge energy in the presence of a substrate is lower than that for the other two samples (Fe−ABH2 with and without αKG). This indicates a change in the electronic environment of the Fe(II) center in the presence of the substrate. Differences are also observed in the maximal intensity of the rising edge (white line) and also at energies above the edge (e.g., at ∼7160 eV). These differences also reflect changes in the structure of the Fe(II) site upon addition of substrate.[55] The five-coordinate Fe(II) site is in contrast to the known structure of Mn-substituted ABH2, which reveals a six-coordinate Mn(II) site in the ternary complex formed with αKG and substrate.[22]

The reaction sequence in Scheme 2 is distinct from the consensus mechanism (Scheme 1) in that a five-coordinate complex is present in the resting enzyme and is maintained in the catalytic cycle through the formation of the enzyme−substrate complex (vide supra). This implies that Fe−ABH2 uses a mechanism different from that found in other non-heme Fe(II) oxygenases to prevent reductive activation of O_2 prior to formation of the ternary complex.

One possible alternative mechanism would be to use the protein conformation to block access of O_2 to the Fe site and remove the impediment when substrate binds via a protein conformational change. The presence of a five-coordinate Fe(II) site in the resting enzyme (Scheme 2, A) and its maintenance through formation of the ternary complex are not unprecedented in DNA or histone demethylases. The crystal structure of JMJD2A with αKG (no substrate) also reveals a five-coordinate Fe(II) site.[56] An allosteric mechanism also has a precedent in bacterial DNA demethylases. *E. coli* AlkB is a bacterial enzyme that catalyzes demethylation of methylated DNA bases. Like human ABH2, AlkB is a mononuclear non-heme Fe(II) enzyme that utilizes αKG and O_2 to conduct the oxidative demethylation of DNA. Both of these enzymes also utilize the facial 2-His-1-carboxylate motif to bind Fe(II). There are several crystal structures of AlkB available in the literature where Fe(II) has been replaced with Mn(II), Co(II), or Ni(II) in presence of αKG and also in the presence of both αKG and substrate.[22,57−59] All of the metal-substituted AlkB enzymes are catalytically inactive. Comparison of crystal structures of AlkB containing Fe(II), Co(II), or Mn(II) in the presence of both αKG and substrate shows that the positioning of Trp178 and Leu184 is different in the case of Mn(II) or Co(II) than in case of Fe(II).[59,60] In the case of Mn(II) and Co(II), Trp178 blocks the O_2 binding site and Leu184 blocks the O_2 diffusion tunnel.

For Ni(II), the mechanism of ABH2 inhibition is different in three important ways. First, Ni(II) in a ligand environment consisting of the 2-His-1-caboxylate protein binding site and an αKG ligand would not be expected to possess a redox potential capable of reducing O_2.[60−62] Second, the electron density buildup that occurs on the Fe(II) center upon binding of αKG and then substrate is not observed for Ni(II). Third, the ternary complex of Ni(II), the protein, and αKG contains a six-coordinate nickel site (Figure 5) that has no open coordination site for binding O_2. The six-coordinate complex formed with Ni(II) is indistinguishable from the structure of the Mn(II) center in the Mn-substituted enzyme. Thus, inhibition by metal ions other than Fe(II) appears to involve blocking access to the metal via coordination of a sixth ligand, and in the case of Ni(II), both electronic and steric components may be involved.

ASSOCIATED CONTENT

Supporting Information. Tables of EXAFS fits to Fe and Ni *K*-edge data used to select the best-fit models, figures of XANES analyses, and an enzyme activity assay of ABH2. This material is available free of charge via the Internet at http://pubs.acs.org.

AUTHOR INFORMATION

Corresponding Author

*Phone: (413) 545-4876. Fax: (413) 545-4490. E-mail: maroney@chemistry.umass.edu.

Funding Sources

This work was supported by National Institutes of Health Grant ES005512-P30ES000260 (M.C.).

ACKNOWLEDGMENT

The Stanford Synchrotron Radiation Laboratory (SSRL) is a national user facility operated by Stanford University on behalf of the U.S. Department of Energy, Office of Basic Energy Sciences. The SSRL Structural and Molecular Biology Program is supported by the Department of Energy, Office of Biological and Environmental Research, and by the National Institutes of Health, National Center for Research Resources, Biomedical Technology Program.

ABBREVIATIONS

ABH2, α-ketoglutarate-dependent dioxygenase AlkB human homologue 2; αKG, 2-oxopentanedioic acid; BSA, bovine serum albumin; ICP-OES, inductively coupled plasma-optical emission spectroscopy; PCD, protocatechuate 3,4-dioxygenase; EXAFS, extended X-ray absorption fine structure; XANES, X-ray absorption near-edge structure; XAS, X-ray absorption spectroscopy.

REFERENCES

(1) Martienssen, R. A., and Colot, V. (2001) DNA methylation and epigenetic inheritance in plants and filamentous fungi. *Science 293*, 1070–1074.

(2) Bird, A. (2002) DNA methylation patterns and epigenetic memory. *Gene Dev. 16*, 6–21.

(3) Tariq, M., and Paszkowski, J. (2004) DNA and histone methylation in plants. *Trends Genet. 20*, 244–251.

(4) Bender, J. (2004) DNA methylation and epigenetics. *Annu. Rev. Plant Biol. 55*, 41–68.

(5) Chan, S. W. L., Henderson, I. R., and Jacobsen, S. E. (2005) Gardening the genome: DNA methylation in *Arabidopsis thaliana*. *Nat. Rev. Genet. 6*, 351–360.

(6) Wood, R. D., Mitchell, M., Sgouros, J., and Lindahl, T. (2001) Human DNA repair genes. *Science 291*, 1284–1289.

(7) Aas, P. A., Otterlei, M., Falnes, P. O., Vagbo, C. B., Skorpen, F., Akbari, M., Sundheim, O., Bjoras, M., Slupphaug, G., Seeberg, E., and Krokan, H. E. (2003) Human and bacterial oxidative demethylases repair alkylation damage in both RNA and DNA. *Nature 421*, 859–863.

(8) Rydberg, B., and Lindahl, T. (1982) Non-enzymatic methylation of DNA by the intracellular methyl group donor S-adenosyl-L-methionine is a potentially mutagenic reaction. *EMBO J. 1*, 211–216.

(9) Sedgwick, B. (2004) Repairing DNA-methylation damage. *Nat. Rev. Mol. Cell Biol. 5*, 148–157.

(10) Drablos, F., Feyzi, E., Aas, P. A., Vaagbo, C. B., Kavli, B., Bratlie, M. S., Pena-Diaz, J., Otterlei, M., Slupphaug, G., and Krokan, H. E. (2004) Alkylation damage in DNA and RNA: Repair mechanisms and medical significance. *DNA Repair 3*, 1389–1407.

(11) Lindahl, T., Sedgwick, B., Sekiguchi, M., and Nakabeppu, Y. (1988) Regulation and expression of the adaptive response to alkylating agents. *Annu. Rev. Biochem. 57*, 133–157.

(12) Lee, D. H., Jin, S. G., Cai, S., Chen, Y., Pfeifer, G. P., and O'Connor, T. R. (2005) Repair of methylation damage in DNA and RNA by mammalian AlkB homologues. *J. Biol. Chem. 280*, 39448–39459.

(13) Ringvoll, J., Nordstrand, L. M., Vagbo, C. B., Talstad, V., Reite, K., Aas, P. A., Lauritzen, K. H., Liabakk, N. B., Bjork, A., Doughty, R. W., Falnes, P. O., Krokan, H. E., and Klungland, A. (2006) Repair deficient mice reveal mABH2 as the primary oxidative demethylase for repairing 1meA and 3meC lesions in DNA. *EMBO J. 25*, 2189–2198.

(14) Duncan, T., Trewick, S. C., Koivisto, P., Bates, P. A., Lindahl, T., and Sedgwick, B. (2002) Reversal of DNA alkylation damage by two human dioxygenases. *Proc. Natl. Acad. Sci. U.S.A. 99*, 16660–16665.

(15) Bollinger, J. M., Price, J. C., Hoffart, L. M., Barr, E. W., and Krebs, C. (2005) Mechanism of taurine:α-ketoglutarate dioxygenase (TauD) from *E. coli*. *Eur. J. Inorg. Chem.*, 4245–4254.

(16) Hausinger, R. P. (2004) Fe(II)/α-ketoglutarate-dependent hydroxylases and related enzymes. *Crit. Rev. Biochem. Mol. Biol. 39*, 21–68.

(17) Roach, P. L., Clifton, I. J., Hensgens, C. M. H., Shibata, N., Schofield, C. J., Hajdu, J., and Baldwin, J. E. (1997) Structure of isopenicillin N synthase complexed with substrate and the mechanism of penicillin formation. *Nature 387*, 827–830.

(18) Koehntop, K. D., Emerson, J. P., and Que, L. (2005) The 2-His-1-carboxylate facial triad: A versatile platform for dioxygen activation by mononuclear non-heme iron(II) enzymes. *J. Biol. Inorg. Chem. 10*, 87–93.

(19) Neidig, M. L., Brown, C. D., Kavana, M., Choroba, O. W., Spencer, J. B., Moran, G. R., and Solomon, E. I. (2006) Spectroscopic and electronic structure studies of the role of active site interactions in the decarboxylation reaction of α-keto acid-dependent dioxygenases. *J. Inorg. Biochem. 100*, 2108–2116.

(20) Neidig, M. L., and Solomon, E. I. (2005) Structure-function correlations in oxygen activating non-heme iron enzymes. *Chem. Commun.*, 5843–5863.

(21) Neidig, M. L., Brown, C. D., Light, K. M., Fujimori, D. G., Nolan, E. M., Price, J. C., Barr, E. W., Bollinger, J. M., Krebs, C., Walsh, C. T., and Solomon, E. I. (2007) CD and MCD of CytC3 and taurine

dioxygenase: Role of the facial triad in α-KG-dependent oxygenases. *J. Am. Chem. Soc. 129*, 14224–14231.

(22) Yang, C. G., Yi, C. Q., Duguid, E. M., Sullivan, C. T., Jian, X., Rice, P. A., and He, C. (2008) Crystal structures of DNA/RNA repair enzymes AlkB and ABH2 bound to dsDNA. *Nature 452*, 961–964.

(23) Chen, H. B., Giri, N. C., Zhang, R. H., Yamane, K., Zhang, Y., Maroney, M., and Costa, M. (2010) Nickel ions inhibit histone demethylase JMJD1A and DNA repair enzyme ABH2 by replacing the ferrous iron in the catalytic centers. *J. Biol. Chem. 285*, 7374–7383.

(24) Lee, Y. W., Broday, L., and Costa, M. (1998) Effects of nickel on DNA methyltransferase activity and genomic DNA methylation levels. *Mutat. Res. 415*, 213–218.

(25) Zingg, J. M., and Jones, P. A. (1997) Genetic and epigenetic aspects of DNA methylation on genome expression, evolution, mutation and carcinogenesis. *Carcinogenesis 18*, 869–882.

(26) Smith, P. K. et al. (1985) Measurement of protein using bicinchoninic acid. *Anal. Biochem. 150*, 76–85.

(27) Roy, T. W., and Bhagwat, A. S. (2007) Kinetic studies of *E. coli* AlkB using a new fluorescence-based assay for DNA demethylation. *Nucleic Acids Res. 35*, e147.

(28) Leitch, S., Bradley, M. J., Rowe, J. L., Chivers, P. T., and Maroney, M. J. (2007) Nickel-specific response in the transcriptional regulator, *E. coli* NikR. *J. Am. Chem. Soc. 129*, 5085–5095.

(29) Padden, K. M., Krebs, J. F., MacBeth, C. E., Scarrow, R. C., and Borovik, A. S. (2001) Immobilized metal complexes in porous organic hosts: Development of a material for the selective and reversible binding of nitric oxide. *J. Am. Chem. Soc. 123*, 1072–1079.

(30) Webb, S. M. (2005) SIXpack: A graphical user interface for XAS analysis using IFEFFIT. *Phys. Scr. T115*, 1011–1014.

(31) Ankudinov, A. L., Ravel, B., Rehr, J. J., and Conradson, S. D. (1998) Real-space multiple-scattering calculation and interpretation of X-ray-absorption near-edge structure. *Phys. Rev. B: Condens. Matter Mater. Phys. 58*, 7565–7576.

(32) Newville, M. (2001) EXAFS analysis using FEFF and FEFFIT. *J. Synchrotron Radiat. 8*, 96–100.

(33) Zabinsky, S. I., Rehr, J. J., Ankudinov, A., Albers, R. C., and Eller, M. J. (1995) Multiple-Scattering Calculations of X-ray-Absorption Spectra. *Phys. Rev. B: Condens. Matter Mater. Phys. 52*, 2995–3009.

(34) Colpas, G. J., Maroney, M. J., Bagyinka, C., Kumar, M., Willis, W. S., Suib, S. L., Baidya, N., and Mascharak, P. K. (1991) X-ray spectroscopic studies of nickel-complexes, with application to the structure of nickel sites in hydrogenases. *Inorg. Chem. 30*, 920–928.

(35) Randall, C. R., Shu, L. J., Chiou, Y. M., Hagen, K. S., Ito, M., Kitajima, N., Lachicotte, R. J., Zang, Y., and Que, L. (1995) X-ray-absorption pre-edge studies of high-spin iron(II) complexes. *Inorg. Chem. 34*, 1036–1039.

(36) Westre, T. E., Kennepohl, P., DeWitt, J. G., Hedman, B., Hodgson, K. O., and Solomon, E. I. (1997) A multiplet analysis of Fe K-edge 1s → 3d pre-edge features of iron complexes. *J. Am. Chem. Soc. 119*, 6297–6314.

(37) Cosper, N. J., Stalhandske, C. M. V., Saari, R. E., Hausinger, R. P., and Scott, R. A. (1999) X-ray absorption spectroscopic analysis of Fe(II) and Cu(II) forms of a herbicide-degrading α-ketoglutarate dioxygenase. *J. Biol. Inorg. Chem. 4*, 122–129.

(38) Costello, A., Periyannan, G., Yang, K. W., Crowder, M. W., and Tierney, D. L. (2006) Site-selective binding of Zn(II) to metallo-β-lactamase L1 from *Stenotrophomonas maltophilia*. *J. Biol. Inorg. Chem. 11*, 351–358.

(39) Costello, A. L., Sharma, N. P., Yang, K. W., Crowder, M. W., and Tierney, D. L. (2006) X-ray absorption spectroscopy of the zinc-binding sites in the class B2 metallo-β-lactamase ImiS from *Aeromonas veronii* bv. *sobria*. *Biochemistry 45*, 13650–13658.

(40) Kim, Y. J., Feng, X. D., and Lippard, S. J. (2007) Synthesis, structure, and properties of a mixed-valent triiron complex of tetramethyl reductic acid, an ascorbic acid analogue, and its relationship to a functional non-heme iron oxidation catalyst system. *Inorg. Chem. 46*, 6099–6107.

(41) Wasinger, E. C., Davis, M. I., Pau, M. Y. M., Orville, A. M., Zaleski, J. M., Hedman, B., Lipscomb, J. D., Hodgson, K. O., and Solomon, E. I. (2003) Spectroscopic studies of the effect of ligand donor strength on the Fe-NO bond in intradiol dioxygenases. *Inorg. Chem. 42*, 365–376.

(42) Westre, T. E., Kennepohl, P., DeWitt, J. G., Hedman, B., Hodgson, K. O., and Solomon, E. I. (1997) A multiplet analysis of Fe K-edge 1s → 3d pre-edge features of iron complexes. *J. Am. Chem. Soc. 119*, 6297–6314.

(43) Shan, X., Rohde, J. U., Koehntop, K. D., Zhou, Y., Bukowski, M. R., Costas, M., Fujisawa, K., and Que, L. (2007) X-ray absorption spectroscopic studies of high-spin nonheme (alkylperoxo)iron(III) intermediates. *Inorg. Chem. 46*, 8410–8417.

(44) Davis, M. I., Wasinger, E. C., Westre, T. E., Zaleski, J. M., Orville, A. M., Lipscomb, J. D., Hedman, B., Hodgson, K. O., and Solomon, E. I. (1999) Spectroscopic investigation of reduced protocatechuate 3,4-dioxygenase: Charge-induced alterations in the active site iron coordination environment. *Inorg. Chem. 38*, 3676–3683.

(45) Que, L., and Ho, R. Y. N. (1996) Dioxygen activation by enzymes with mononuclear non-heme iron active sites. *Chem. Rev. 96*, 2607–2624.

(46) Khan, M. M. T., and Martell, A. E. (1967) Metal ion and metal chelate catalyzed oxidation of ascorbic acid by molecular oxygen. I. cupric and ferric ion catalyzed oxidation. *J. Am. Chem. Soc. 89*, 4176–4185.

(47) Khan, M. M. T., and Martell, A. E. (1967) Metal ion and metal chelate catalyzed oxidation of ascorbic acid by molecular oxygen. II. Cupric and ferric chelate catalyzed oxidation. *J. Am. Chem. Soc. 89*, 7104–7111.

(48) Yu, L., Wang, Y., Huang, S., Wang, J. J., Deng, Z. Q., Zhang, Q., Wu, W., Zhang, X. L., Liu, Z., Gong, W. M., and Chen, Z. Z. (2010) Structural insights into a novel histone demethylase PHF8. *Cell Res. 20*, 166–173.

(49) O'Brien, J. R., Schuller, D. J., Yang, V. S., Dillard, B. D., and Lanzilotta, W. N. (2003) Substrate-induced conformational changes in *Escherichia coli* taurine/α-ketoglutarate dioxygenase and insight into the oligomeric structure. *Biochemistry 42*, 5547–5554.

(50) Wong, C., Fujimori, D. G., Walsh, C. T., and Drennan, C. L. (2009) Structural Analysis of an Open Active Site Conformation of Nonheme Iron Halogenase CytC3. *J. Am. Chem. Soc. 131*, 4872–4879.

(51) Zhang, Z. H., Ren, J. S., Stammers, D. K., Baldwin, J. E., Harlos, K., and Schofield, C. J. (2000) Structural origins of the selectivity of the trifunctional oxygenase clavaminic acid synthase. *Nat. Struct. Biol. 7*, 127–133.

(52) Costas, M., Mehn, M. P., Jensen, M. P., and Que, L. (2004) Dioxygen activation at mononuclear nonheme iron active sites: Enzymes, models, and intermediates. *Chem. Rev. 104*, 939–986.

(53) Hanauskeabel, H. M., and Gunzler, V. (1982) A stereochemical concept for the catalytic mechanism of prolylhydroxylase: Applicability to classification and design of inhibitors. *J. Theor. Biol. 94*, 421–455.

(54) Solomon, E. I., Brunold, T. C., Davis, M. I., Kemsley, J. N., Lee, S. K., Lehnert, N., Neese, F., Skulan, A. J., Yang, Y. S., and Zhou, J. (2000) Geometric and electronic structure/function correlations in non-heme iron enzymes. *Chem. Rev. 100*, 235–349.

(55) Chow, M. S., Eser, B. E., Wilson, S. A., Hodgson, K. O., Hedman, B., Fitzpatrick, P. F., and Solomon, E. I. (2009) Spectroscopy and kinetics of wild-type and mutant tyrosine hydroxylase: Mechanistic insight into O_2 activation. *J. Am. Chem. Soc. 131*, 7685–7698.

(56) Chen, Z. Z., Zang, J. Y., Whetstine, J., Hong, X., Davrazou, F., Kutateladze, T. G., Simpson, M., Mao, Q. L., Pan, C. H., Dai, S. D., Hagman, J., Hansen, K., Shi, Y., and Zhang, G. Y. (2006) Structural insights into histone demethylation by JMJD2 family members. *Cell 125*, 691–702.

(57) Yu, B., Edstrom, W. C., Benach, J., Hamuro, Y., Weber, P. C., Gibney, B. R., and Hunt, J. F. (2006) Crystal structures of catalytic complexes of the oxidative DNA/RNA repair enzyme AlkB. *Nature 439*, 879–884.

(58) Yu, B., and Hunt, J. F. (2009) Enzymological and structural studies of the mechanism of promiscuous substrate recognition by the oxidative DNA repair enzyme AlkB. *Proc. Natl. Acad. Sci. U.S.A. 106*, 14315–14320.

(59) Holland, P. J., and Hollis, T. (2010) Structural and mutational analysis of *E. coli* AlkB provides insight into substrate specificity and DNA damage searching. *PLoS One 5*, e8680.

(60) Mirza, S. A., Day, R. O., and Maroney, M. J. (1996) Oxidation of a dimeric nickel thiolate complex with O_2. *Inorg. Chem. 35*, 1992–1995.

(61) Grapperhaus, C. A., and Darensbourg, M. Y. (1998) Oxygen capture by sulfur in nickel thiolates. *Acc. Chem. Res. 31*, 451–459.

(62) Goldcamp, M. J., Robison, S. E., Bauer, J. A. K., and Baldwin, M. J. (2002) Oxygen reactivity of a nickel(II)-polyoximate complex. *Inorg. Chem. 41*, 2307–2309.